Geophysical Journal International

Geophys. J. Int. (2011) **186,** 45–58 doi: 10.1111/j.1365-246X.2011.05023.x

Continental and oceanic crustal structure of the Pampean flat slab region, western Argentina, using receiver function analysis: new high-resolution results

Christine R. Gans,[1] Susan L. Beck,[1] George Zandt,[1] Hersh Gilbert,[2] Patricia Alvarado,[3] Megan Anderson,[4] and Lepolt Linkimer[1]

[1]*Department of Geosciences, University of Arizona, Tucson, AZ* 85721*, USA. E-mail: cgans@email.arizona.edu*
[2]*Department of Earth & Atmospheric Sciences, Purdue University, West Lafayette, IN* 47907*, USA*
[3]*Dpto. de Geofisica y Astronomía, FCEFN – Universidad Nacional de San Juan-CONICET, Meglioli* 1160 *S* (5400)*, San Juan, Argentina*
[4]*Department of Geology, Colorado College, Colorado Springs, CO* 80903*, USA*

Accepted 2011 March 19. Received 2011 March 17; in original form 2010 December 2

SUMMARY

The Pampean flat slab of central Chile and Argentina (30°–32°S) has strongly influenced Cenozoic tectonics in western Argentina, which contains both the thick-skinned, basement-cored uplifts of the Sierras Pampeanas and the thin-skinned Andean Precordillera fold and thrust belt. In this region of South America, the Nazca Plate is subducting nearly horizontally beneath the South American Plate at ∼100 km depth. To gain a better understanding of the deeper structure of this region, including the transition from flat to 'normal' subduction to the south, three IRIS-PASSCAL arrays of broad-band seismic stations have been deployed in central Argentina. Using the dense SIEMBRA array, combined with the broader CHARGE and ESP arrays, the flat slab is imaged for the first time in 3-D detail using receiver function (RF) analysis. A distinct pair of RF arrivals consisting of a negative pulse that marks the top of the oceanic crust, followed by a positive pulse, which indicates the base of the oceanic crust, can be used to map the slab's structure. Depths to Moho and oceanic crustal thicknesses estimated from RF results provide new, more detailed regional maps. An improved depth to continental Moho map shows depths of more than 70 km in the main Cordillera and ∼50 km in the western Sierras Pampeanas, that shallow to ∼35 km in the eastern Sierras Pampeanas. Depth to Moho contours roughly follow terrane boundaries. Offshore, the hotspot seamount chain of the Juan Fernández Ridge (JFR) is thought to create overthickened oceanic crust, providing a mechanism for flat slab subduction. By comparing synthetic RFs, based on various structures, to the observed RF signal we determine that the thickness of the oceanic crust at the top of the slab averages at least ∼13–19 km, supporting the idea of a moderately overthickened crust to provide the additional buoyancy for the slab to remain flat. The overthickened region is broader than the area directly aligned with the path of the JFR, however, and indicates, along with the slab earthquake locations, that the flat slab area is wider than the JFR volcanic chain observed in the offshore bathymetry. Further, RFs indicate that the subducted oceanic crust in the region directly along the path of the subducted ridge is broken by trench-parallel faults. One explanation for these faults is that they are older structures within the oceanic crust that were created when the slab subducted. Alternatively, it is possible that faults formed recently from tectonic underplating caused by increased interplate coupling in the flat slab region.

Key words: Seismicity and tectonics; Body waves; Continental margins: convergent; Dynamics of lithosphere and mantle; Crustal structure; South America.

INTRODUCTION AND TECTONIC BACKGROUND

The western margin of South America between 30° and 32°S is characterized by the flat slab subduction of the ∼43 Ma oceanic Nazca Plate beneath the continental South American Plate at a rate of ∼7.5 cm yr^{-1}, with an azimuth of ∼74° (DeMets *et al.* 2010). The low angle subduction has prevented magmatism in the area since the late Miocene, due to reduced mantle flow above the subducting slab, and spatially correlates with the formation of both thick-skinned [Sierras Pampeanas (SP)] basement-cored uplifts and the thin-skinned (Andean Precordillera) fold and thrust belt within

the region (e.g. Jordan *et al.* 1983; Kay *et al.* 1991; Ramos *et al.* 1996). Total crustal shortening is believed to range between 150 and 170 km (Allmendinger *et al.* 1990). The flat slab follows the path of the subducting Juan Fernández Ridge (JFR), a hot spot seamount chain on the Nazca Plate (Pilger 1981), and its geometry has been determined using both global seismicity data sets (Cahill & Isacks 1992) and relocated slab earthquakes using local array data (Anderson *et al.* 2007). Several names have been assigned to the flab slab in this region: the Chile–Argentina flat slab, the Chilean flat slab, the Central Andean flat slab and the Pampean flat slab; in this paper we will use the term Pampean flat slab to describe the lithospheric analysis on the Argentinean side. The Pampean flat slab has been of particular interest to scientists working in the western United States, as the present-day South American geometry is often considered an analogue, although on a much smaller scale, to the flat slab subduction that occurred during the Laramide orogeny in the United States (e.g. Jordan & Allmendinger 1986; Saleeby 2003; DeCelles 2004).

Flat slab subduction is found in approximately 10 per cent of subduction zones worldwide (Gutscher *et al.* 2000b). In such regions, the subducting slab changes dip from normal (steeply dipping at $\sim 30^{\circ}$) to subhorizontal. The depth at which slabs flatten, and their horizontal extent from the trench, varies between subduction zones (e.g. Gutscher *et al.* 2000b). In our region of study, the Nazca slab initially dips underneath the continent and flattens at a depth of approximately 100 km, remaining almost horizontal for ∼300 km before descending more steeply into the mantle (Cahill & Isacks 1992; Gutscher *et al.* 2000b; Fig. 1). There are many proposed mechanisms for flab slab subduction, including: (1) subduction of lithosphere of increased buoyancy resulting from its young age or the subduction of overthickened oceanic crust (as in a plateau or ridge), (2) overthrusting of the subducting plate and (3) suction forces between the slab and the overriding plate (e.g. Pilger 1981; McGeary *et al.* 1985; Gutscher *et al.* 2000b; van Hunen *et al.* 2004; Guillaume *et al.* 2009). The area of the Pampean flat slab may meet both the first and second criteria, as the JFR may provide additional buoyancy (Yáñez *et al.* 2001) and the South American Plate is overriding the Nazca Plate at approximately 1 cm yr^{-1} in the direction of $\sim 350^{\circ}$ (Gripp & Gordon 2002). Yáñez *et al.* (2002) predict a mean oceanic crustal thickness of 20–22 km for the already subducted portion of the JFR, based on gravity modelling. Using seismic reflection data, Kopp *et al.* (2004) did not find overthickened crust in the offshore portion of the JFR, however, instead only moderately thick (∼8–10 km) oceanic crust. They attribute the buoyancy of the Nazca slab to hydration of the crust and upper mantle portion of the slab, rather than it having overthickened oceanic crust. Martinod *et al.* (2005) conducted analogue experiments involving subduction of oceanic plateaus and concluded that the current size of the JFR is not large enough to initiate flat slab subduction, but that the previous trench-parallel subduction of a portion of the JFR (around 14–10 Ma) could explain the present day geometry. One of the aims of this paper is to use receiver function (RF) analysis to determine whether the already subducted portion of the JFR is overthickened and how much buoyancy it could then add to the slab.

There were three major episodes of extension in the upper South American Plate, which weakened the crust (Ramos 2009) and contributed to the more recent pattern of Cenozoic crustal deformation. The first episode was during the late Paleozoic, where pull-apart rifting in the southwest SP likely controlled dextral faulting along previously existing structures associated with oblique subduction (Rapela *et al*. 1998; Ramos *et al.* 2002). During Late Triassic-Early Jurassic extension, there was faulting that reached the western edge of the Pampia terrane (which would later become the location of the SP). The third event was during the Early Cretaceous, when normal faulting shifted eastward due to the opening of the South Atlantic (Ramos *et al.* 2002). This extension, controlled by older basement fabrics and crustal-scale structures, influenced the subsequent uplift, creation and distribution of regional normal faults in the eastern

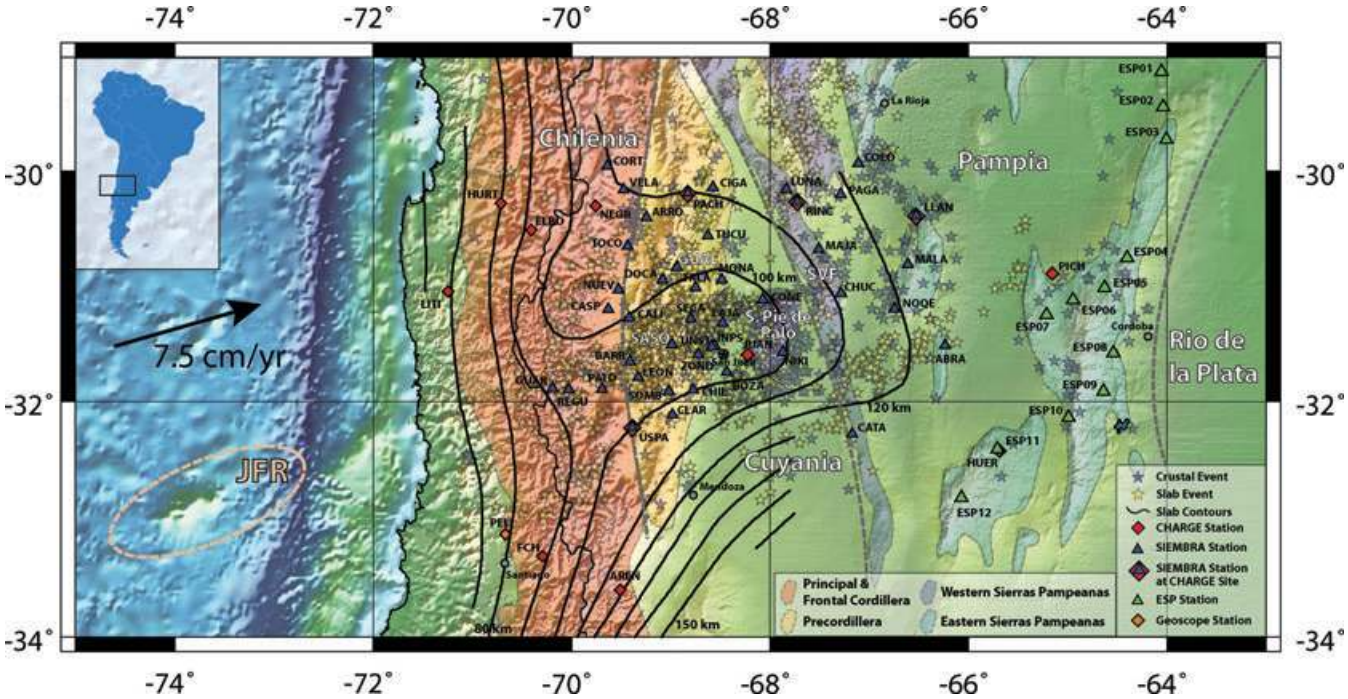

Figure 1. Location map with broad-band seismic stations used in this study. Region of high seismicity outlines the flat slab. Slab contours from Anderson *et al.* (2007). Morphological provinces discussed in text are outlined; terrane boundaries are dashed grey lines (see text for details). SVF, Sierra de Valle Fértil; JFR, Juan Fernández Ridge.

Sierras Pampeanas (ESP, Ramos *et al.* 2002). There have also been interlaced episodes of compression, when, according to some authors, the Pampia and the Cuyania terranes accreted onto the Rio de la Plata craton, during the Mesoproterozoic and the middle Ordovician, respectively (Ramos *et al.* 2010). Most recently, compression during the Cenozoic built the modern Andes and uplifted the SP. While the exact boundaries between terranes/cratonic blocks and the timing of their collisions are still debated, these sutures have had a strong influence on the Cenozoic tectonics of the SP region (e.g. Ramos *et al.* 2002; Rapela *et al.* 2007).

The region is generally divided into four main morphological and structural provinces, developed in the last ∼25 Ma of compression: the Principal Cordillera, Frontal Cordillera, Precordillera and SP (Fig. 1). The Principal Cordillera, consisting of Mesozoic marine deposits, is characterized by thick-skinned tectonics in the northern and southern segments, and thin-skinned tectonics in the central region (Ramos *et al.* 1996). The rigid block of the expansive Frontal Cordillera contains Paleozoic-Triassic magmatic rocks, whereas the shorter N–S span of the fold-and-thrust belt of the Precordillera consists of Paleozoic carbonate platforms (Ramos *et al.* 1996). The SP to the east are composed of a series of crystalline basement-cored Precambrian-Early Paleozoic rocks, mostly formed starting ∼6 Ma, and separated by basins (Jordan & Allmendinger 1986; Kay & Abbruzzi 1996). The Sierra de Pie de Palo, one of the westernmost basement-cored uplifts of the SP, is a region with increased seismic activity, which terminates to the east at the boundary between Pampia and the Cuyania terrane (e.g. Gutscher 2002; Alvarado *et al.* 2005; Fig. 1). Magmatic evidence suggests that the subducting Pampean slab began to shallow in this area around 18 Ma and obtained its present-day horizontal state by 7 Ma (Yáñez *et al.* 2001; Kay & Mpodozis 2002). Arc magmatism migrated progressively eastward, shutting off completely in the Main Cordillera and Precordillera between 7 and 6 Ma (Kay & Abbruzzi 1996), and in the SP between ∼4.7 and 2 Ma (Gordillo & Linares 1981; Kay & Gordillo 1994; Urbina *et al.* 1997).

To better constrain the crust and upper mantle structure in the transition region between flat slab and normal subduction to the south, several arrays of passive source seismic instruments were deployed in Chile and west-central Argentina (e.g. CHARGE, 2000–2002; SIEMBRA, 2007–2009; ESP, 2008–2010). Broad-band seismometers were initially deployed at 24 sites in central Chile and Argentina (Chile Argentina Geophysical Experiment—CHARGE). While results from this initial broad-scale deployment delineated first-order larger-scale structure, such as thick crust and a very weak Moho converted phase in the western SP transitioning to thinner crust and a strong conversion from the shallower Moho in the ESP (Fromm *et al.* 2004; Alvarado *et al.* 2005; Gilbert *et al.* 2006), a denser array was needed to obtain higher-resolution images of the crust and upper mantle. To this end, two more broad-band arrays were deployed in Argentina, beginning in 2007 (Fig. 1). The Sierras pampeanas Experiment using a Multicomponent Broad-band Array (SIEMBRA), a joint project between the University of Arizona, USA, the Universidad Nacional de San Juan and the Instituto Nacional de Prevención Sísmica, Argentina, comprised 44 sites distributed directly over the flat slab and surrounding region. The ESP experiment, a collaboration between Purdue University and Colorado College, USA, and the Universidad Nacional de San Juan and Universidad Nacional de Córdoba, Argentina, contained 12 seismometers and was designed to investigate the mountain building processes around the Sierra de Córdoba, basement-cored uplifts located in the easternmost ranges of the SP.

PREVIOUS RF SLAB-IMAGING STUDIES

There have been multiple studies of subducting slabs using RFs, although none have obtained highly detailed 3-D images in a flat slab region. In Alaska, Abers *et al.* (2006) plotted RF cross-sections, perpendicular to the trench, that imaged the normally dipping subducting slab down to ∼120 km depth. They found a low velocity layer at the top of the downgoing plate (aligned to, but at a different slope than, the Wadati–Benioff Zone), which they proposed to be the subducting oceanic crust. Such a Low Velocity Zone (LVZ) has also been imaged in other subducting slabs around the world, including those with normal dip: Cascadia (Abers *et al.* 2009), SW Japan (Iidaka *et al.* 2009), Alaska (Ferris *et al.* 2003; Abers *et al.* 2006), Mariana (Tibi *et al.* 2008), Central Andes (Yuan *et al.* 2000) and one with flat slab subduction: Mexico (Perez-Campos *et al.* 2008; Kim *et al.* 2010). For a more extensive reference list on subducting slab LVZs, see Hacker *et al.* (2003b) or Audet *et al.* (2010). This low velocity layer has been variously interpreted as basalt and gabbro metastably extending into the eclogite stability field, hydrous blueschist, a two-layer oceanic crust plus hydrous metasediments, a serpentinized layer above or below the subducting crust, altered oceanic crust, a low-velocity mantle wedge remnant or hydrated oceanic crust at low temperatures (e.g. Helffrich 1996; Hacker *et al.* 2003b; Abers 2005; Kawakatsu & Watada 2007; Perez-Campos *et al.* 2008; Abers *et al.* 2009; Song *et al.* 2009; Kim *et al.* 2010). Most thickness estimates for this LVZ (oceanic crust) range between 7 and 13 km.

DATA AND METHODS

The SIEMBRA project recorded data from 40 broad-band seismometers at 44 sites (Fig. 1). Besides the hundreds of teleseismic events recorded during this period, almost 90 000 local earthquakes were detected. In addition to the SIEMBRA experiment, we incorporated data from the CHARGE and ESP experiments, as well as stations PEL from the Geoscope Global Network and UNSJ from the Universidad Nacional de San Juan. Several of the SIEMBRA stations were relocated at the same sites previously used for the CHARGE stations, to gather additional data at the same location.

We carried out RF analysis on teleseismic *P*, *PP* and *PKP* phases recorded during the three experiments. *P* phases were chosen for large magnitude earthquakes at distances between 25° and 95°, *PP* from 95° to 180° and *PKP* from 110° to 160°. *PP* and *PKP* phases were included in this study to increase the azimuthal distribution of events. Seismograms were initially bandpass filtered from 0.15 to 5 Hz, to remove microseisms and anthropogenic noise, and rotated into radial, tangential and vertical components. RF analysis produces a time-series computed from three-component data, and is sensitive to discontinuities in the crust and upper mantle. We employed an iterative pulse-stripping time-domain deconvolution technique (Ligorria & Ammon 1999), in which the vertical *P*-wave component is deconvolved from the horizontal (radial and tangential) components, and a time-series of Gaussian spikes is formed. RFs contain no information about the source, and the amplitude and timing of the *P–SV* (P_s) conversions are related to the magnitude and depth of discontinuities below the receiver (e.g. Langston 1977; Owens *et al.* 1984). They are most dependent on the thickness and gradient of the shear wave velocity and the density contrasts between layers. By varying the width of the Gaussian

used in the deconvolution, which acts as a low-pass filter, the frequency content of the RFs can be tuned to highlight the features of interest. The minimum wavelength of the signal is therefore restricted, and thus the resolution of recoverable layers is controlled. For this study, we looked at Gaussian values of 0.6, 1, 2.5 and 5, which correspond to low-pass filters of corner frequencies 0.3, 0.5, 1.2 and 2.4 Hz, respectively. Assuming a shear –wave speed of 4 km s^{-1}, RFs corresponding to the aforementioned Gaussian values will only be able to recover layers with thicknesses greater than ∼3, 2, 1 and 0.5 km, respectively. For the results presented here, we chose a Gaussian width of 2.5; our maximum resolution is therefore ∼1 km.

After calculation, the RFs were both normalized (*P*-wave has unit amplitude equal to 1 near 0 s lag time) to increase the amplitudes of P_s conversions after the direct arrival (Gilbert *et al.* 2006) and left unnormalized, and then quality controlled. Amplitude normalization will be addressed in the stacking algorithm discussed below. All RFs were first required to have at least a 70 per cent variance reduction (70 per cent of the signal is fit) in the radial RFs. Next, all RFs were visually inspected, and traces of poor quality (with a negative first arrival, or a significant delay in the direct *P* arrival, for example) were eliminated. Out of the 8104 starting RFs for a Gaussian of 2.5, a total of 5086 normalized RFs passed inspection, and 5082 unnormalized RFs.

Of the 39 SIEMBRA stations that were unique to this deployment, the average number of good-quality RFs per station was 79, with a maximum of 145 at MAJA and a minimum of 14 at UNSJ (which began operation six months prior to the end of the SIEMBRA deployment). Four stations were reinstalled at old CHARGE station locations, and combining data provided an average of 158 good RFs per station. Of the 10 remaining CHARGE stations used in this study, an average of 35 RFs were useable, while for the ESP stations, the average number of good RFs was 84.

Once the RFs were computed, the traces were stacked using the Common Conversion Point (CCP) stacking method (e.g. Dueker & Sheehan 1997; Gilbert & Sheehan 2004), to increase the signal-to-noise ratio and help identify lateral variations in features. By stacking large numbers of RFs from multiple stations, with different near surface effects, we are minimizing the noise in the RFs caused by these effects. Over 5000 traces of Gaussian width 2.5 were incorporated into the final stacks. A mesh of stacking bins was created, and rays within a given bin were stacked together, with a half-bin of sharing on either side. Fig. S1 shows ray density plots, indicating that we have over 150 traces per bin in the flat slab region. We tested various distances for spacing between nodes; for the results presented here, bin centres are separated by 15 km in the SW–NE direction, and 25 km in the NW–SE direction (Fig. 2). Depth increment was a constant 0.5 km. To convert time to depth, we used a *P*-wave velocity of $V_p = 6.2$ km s^{-1} above 50 km depth (averaged Moho), and $V_p = 8.0$ km s^{-1} below. A uniform V_p/V_s of 1.75 throughout the network was assumed. This V_p/V_s value is the same as used in determining slab earthquake locations by Anderson *et al.* (2007) and is an average of the V_p/V_s values determined by Gilbert *et al.* (2006). Assuming a different V_p/V_s across the study area would move the arrivals in the CCP stacks slightly in depth, but they would retain the same overall pattern. Each trace was multiplied by *ir*/*i*, where *ir* is a depth invariant reference angle (20°) and *i* is the incidence angle calculated from *P* slowness. Amplitudes were thus rescaled to correct for variations induced by using earthquakes arriving at difference angles of incidence (e.g. Jones & Phinney 1998).

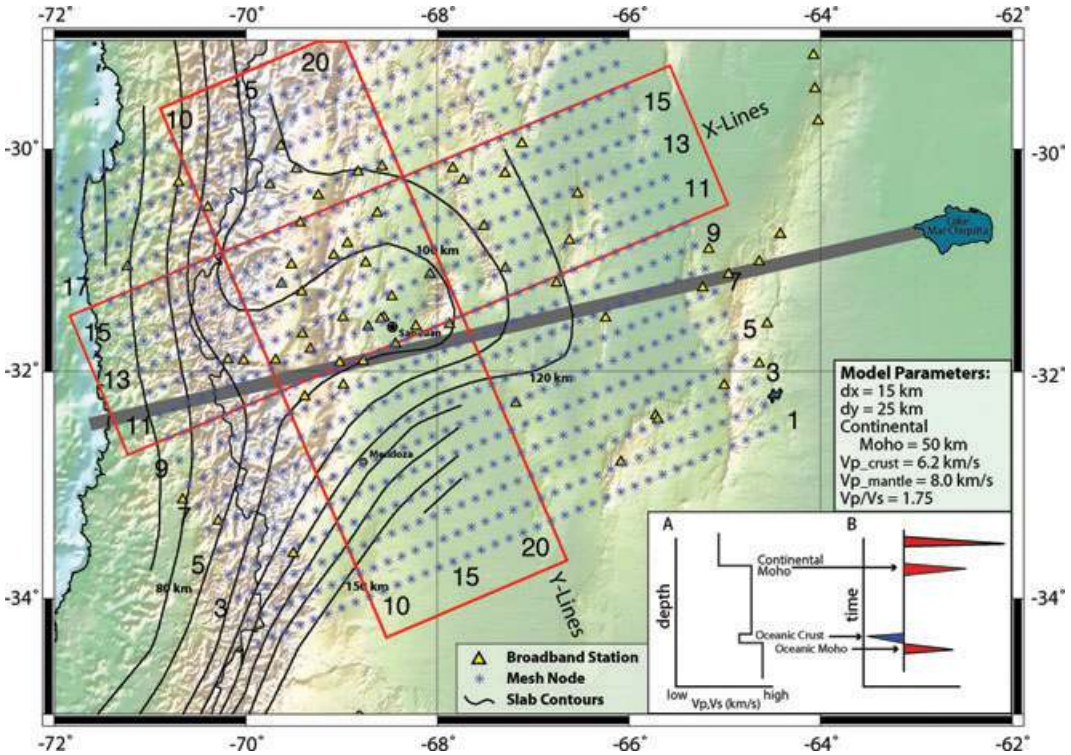

Figure 2. Map with location of CCP Stack mesh, which is aligned along the path of the JFR. Red boxes outline numbered cross-sections shown in Figs 4 and 5. Grey line shows location of crustal x-section shown in Fig. 6. Inset: theoretical receiver function on right (B), with corresponding velocity model on left (A). We are looking for the negative-to-positive arrivals that represent the subducting oceanic slab.

As stated above, we calculated RFs that have been normalized (*P* wave has unit amplitude equal to 1 near 0 s lag time) and unnormalized. Normalization helps to down-weight traces that have exceptionally large amplitudes, which would otherwise 'overpower' traces with smaller overall amplitudes. We have run the CCP stacks using both the unnormalized and normalized data, and all major features remain present. Results are very similar between the normalized and unnormalized data (Fig. S2), with the normalized data containing a few localized regions with high-frequency noise. The stacks using the unnormalized data therefore appear slightly smoother, and so we present the unnormalized data in this paper. Other model parameters are listed in Fig. 2.

It is always prudent to consider whether the arrivals seen in the RFs are primary arrivals, noise or reverberations. One simple method to determine whether an arrival is a primary is to create a radial RF phasing diagram, or moveout plot (Gurrola *et al.* 1994). RFs with similar ray parameter are binned, averaged and finally plotted as a function of slowness. A primary arrival should have positive moveout (with the arrival time of phases increasing with increasing ray parameter), and multiples have negative moveout (arrival time decreasing with increasing ray parameter). Predicted moveout curves for a direct *P* wave of a given layer thickness are calculated using a constant V_p and V_p/V_s. Fig. 3 shows moveout plots for two stations (GUAL and SASO), located directly above the flat slab, calculated at a Gaussian of 2.5. In RFs, the oceanic crust of the subducting slab can be identified as a negative polarity arrival (blue), indicating a decrease in velocity with depth, followed immediately by a positive arrival (red), representing the oceanic Moho (inset, Fig. 2). The negative and positive arrivals that represent the oceanic crust and oceanic Moho, respectively, and their multiples are highlighted in Fig. 3. Portions of both first (PpPhs) and second (PpShs + PsPhs) multiples are visible in this movout plot. For the negative primary of the oceanic crust (black), the first multiple is negative (blue) and the second positive (pink). The opposite is true for the oceanic Moho signal. Layer thicknesses used to calculate the moveout curves are shown to the right, using the same velocity model as the CCP stacks.

RESULTS

The flat slab

CCP RF stacks from the flat slab region are shown in Figs 4 (along-strike of the JFR) and 5 (cross-strike), with line locations in Fig. 2. The mesh is rotated 23° counter-clockwise from horizontal (E–W) to align with the approximate path of the subducting JFR. Due in part to the higher resolution and longer time frame of the SIEMBRA experiment, we are now able to image the subducting flat slab, a key improvement on the previous work of Gilbert *et al.* (2006). A prominent blue-to-red, negative-to-positive conversion representing the oceanic crust is seen at around 80–100 km depth, in the region of the earthquake hypocentre-determined flat slab (Figs 4 and 5). The white circles are single event earthquake locations using the method of Lienert *et al.* (1986), recorded during the SIEMBRA and ESP deployments, with both *P* waves and *S* waves from >12 stations and having station coverage with gaps <180°. The earthquakes are located using the same velocity model used to do the CCP stack migration. A more detailed description of these earthquakes will be presented in a separate paper currently in preparation. Cartoons in Fig. 4 outline the interpreted flat slab and continental Moho, to the extent of our confidence.

One striking observation of the RF results is the varying character of the flat slab directly along the path of the JFR (e.g. X-Line 11) versus slightly to the north, and off-ridge (e.g. X-Line 15). On the northern edge of the flat slab, which aligns to the north of the path of the JFR (X-Line 15), the negative-to-positive conversion is simple and smooth, and does not vary greatly in thickness. Moving to the southeast, the slab signal becomes more complex, and the negative-to-positive conversion appears to become increasingly offset closer to the direct path of the JFR (X-Line 11). This offset can also be seen in the perpendicular NW–SE cross-sections, where the negative-to-positive flat slab arrival in Y-Line 10 shoals along the grid to the northeast, with Y-Line 14 showing the maximum offset. Y-Lines 15 and 16 image the 'healing' of the offset slab signal, and this conversion returns to smooth and flat lying thereafter, until the

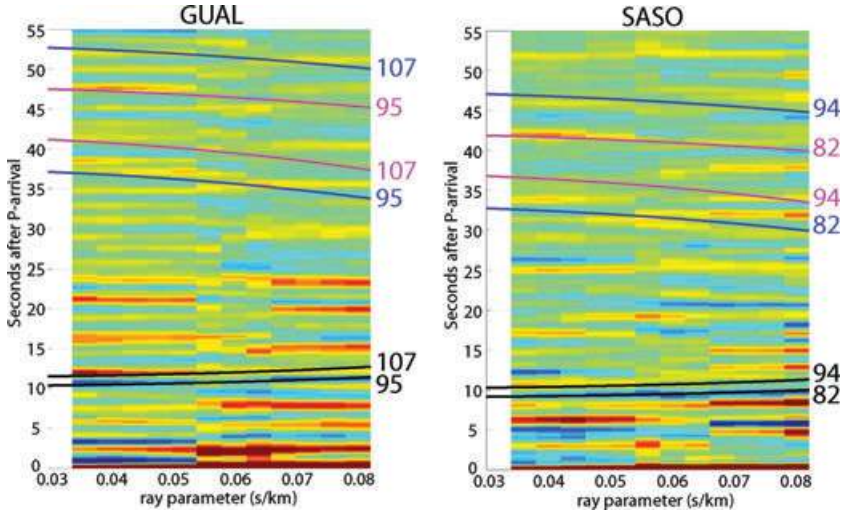

Figure 3. Moveout plots using a Gaussian of 2.5 for two stations located above the Pampean flat slab (see Fig. 1 for station locations), with the oceanic crust and oceanic Moho highlighted by traveltime curves. Solid lines are theoretical traveltime curves. Black lines represent primary arrivals, blue lines represent negative multiple arrivals and pink lines positive multiples. Layer thicknesses (km) are shown to the right. Traveltime curves calculated using the same velocity model as the CCP stacks. See text for details.

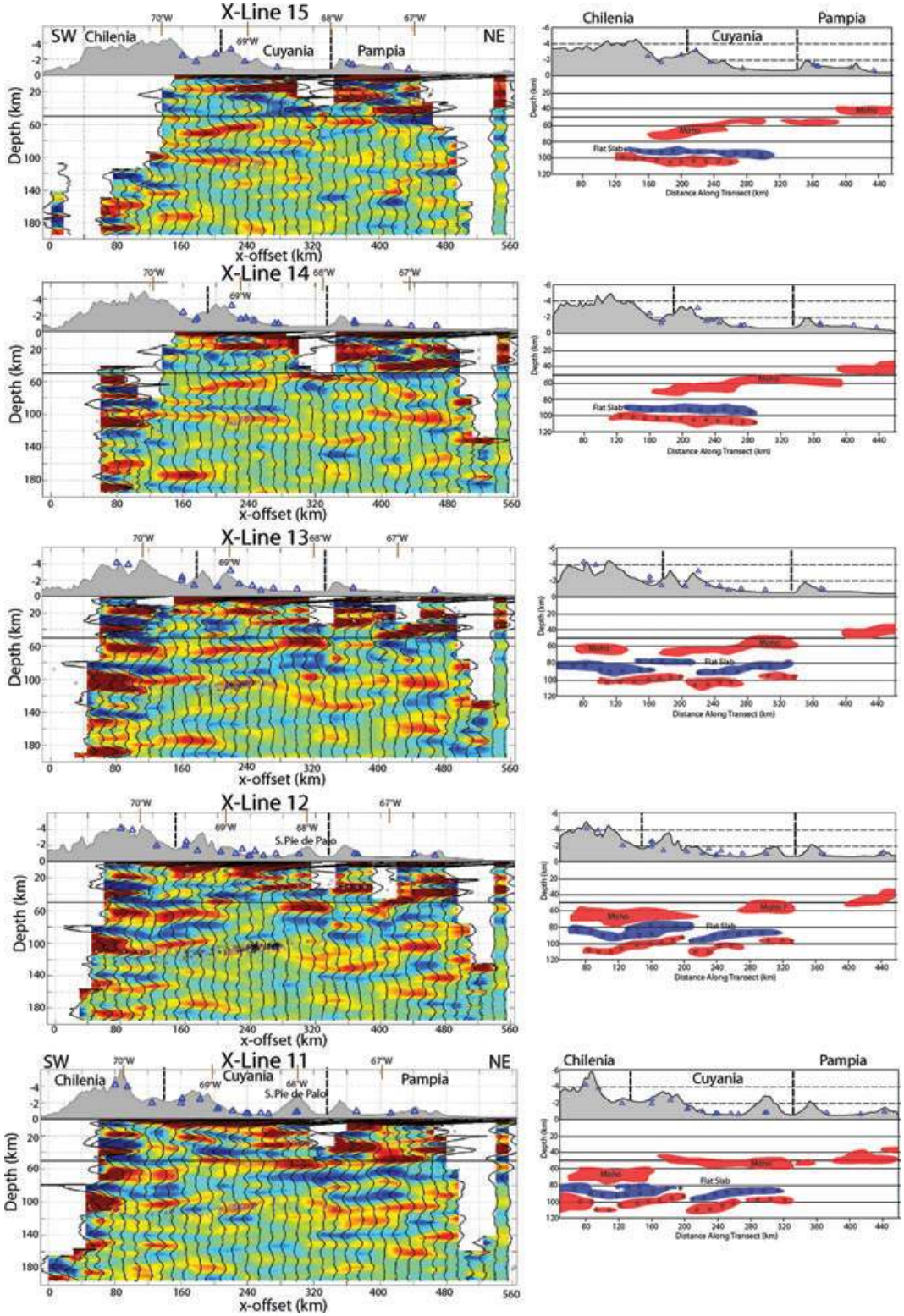

Figure 4. Left-hand side: selected SW–NE CCP Receiver Function Stacks. Note the varying character of the oceanic crust. Continental Moho depths are greatest to the west (∼70–60 km) and shallow to the east (∼40 km). Right-hand side: cartoon of CCP Stacks with continental Moho and flat slab highlighted. Stars represent maximum positive/negative amplitudes of traces. Blue triangles are seismic stations, white circles are earthquakes recorded during the SIEMBRA experiment, vertical black dashed lines mark terrane boundaries suggested by geological studies (see text for details). See Fig. 2 for line locations.

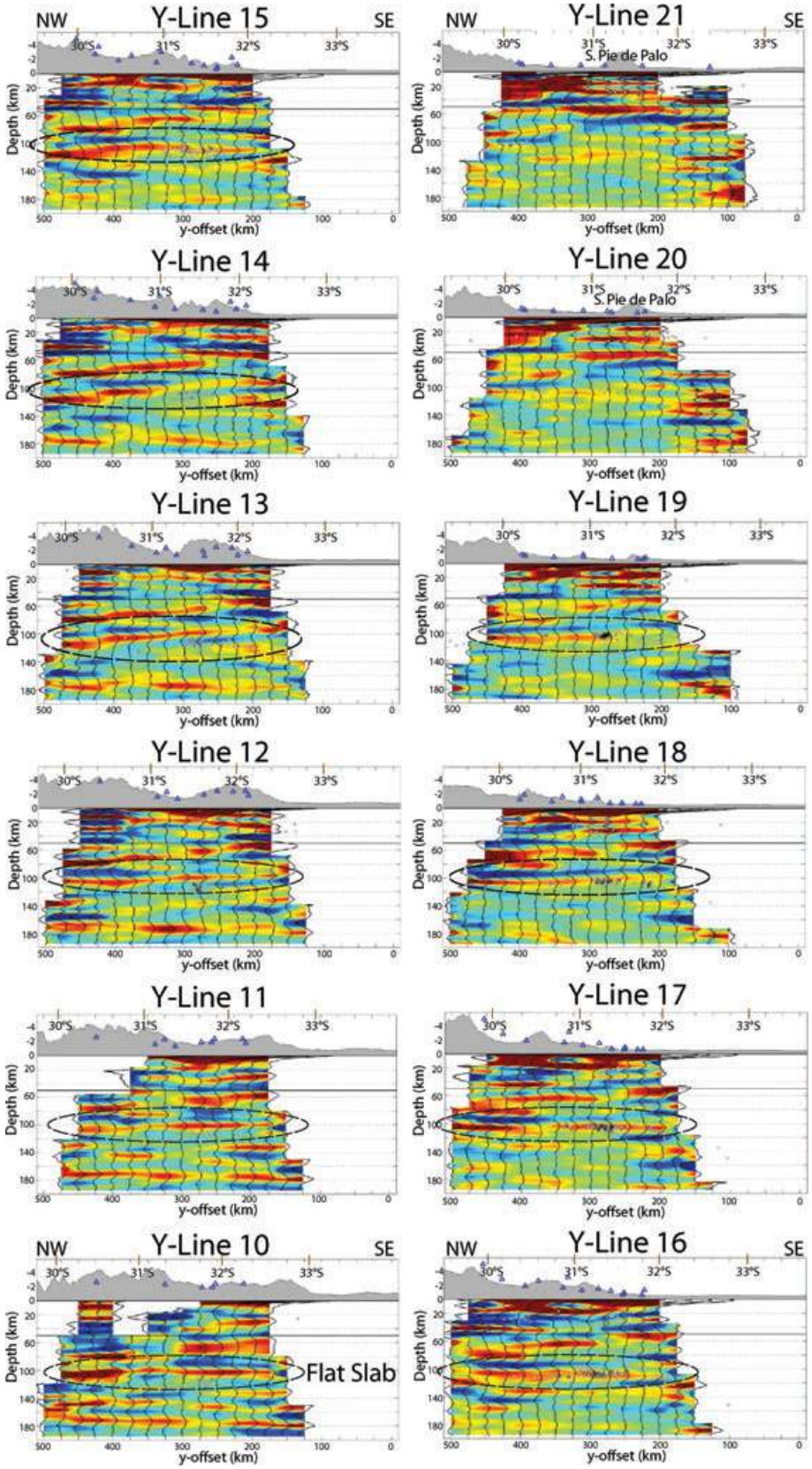

Figure 5. Selected NW–SE CCP Receiver Function Stacks. Note the varying character of the oceanic crust. Flat slab is imaged in most cross-sections (black ellipse), but starts to disappear as the eclogite transition is reached (Y-Line 20). Blue triangles are seismic stations, white circles are earthquakes recorded during the SIEMBRA experiment. See Fig. 2 for line locations.

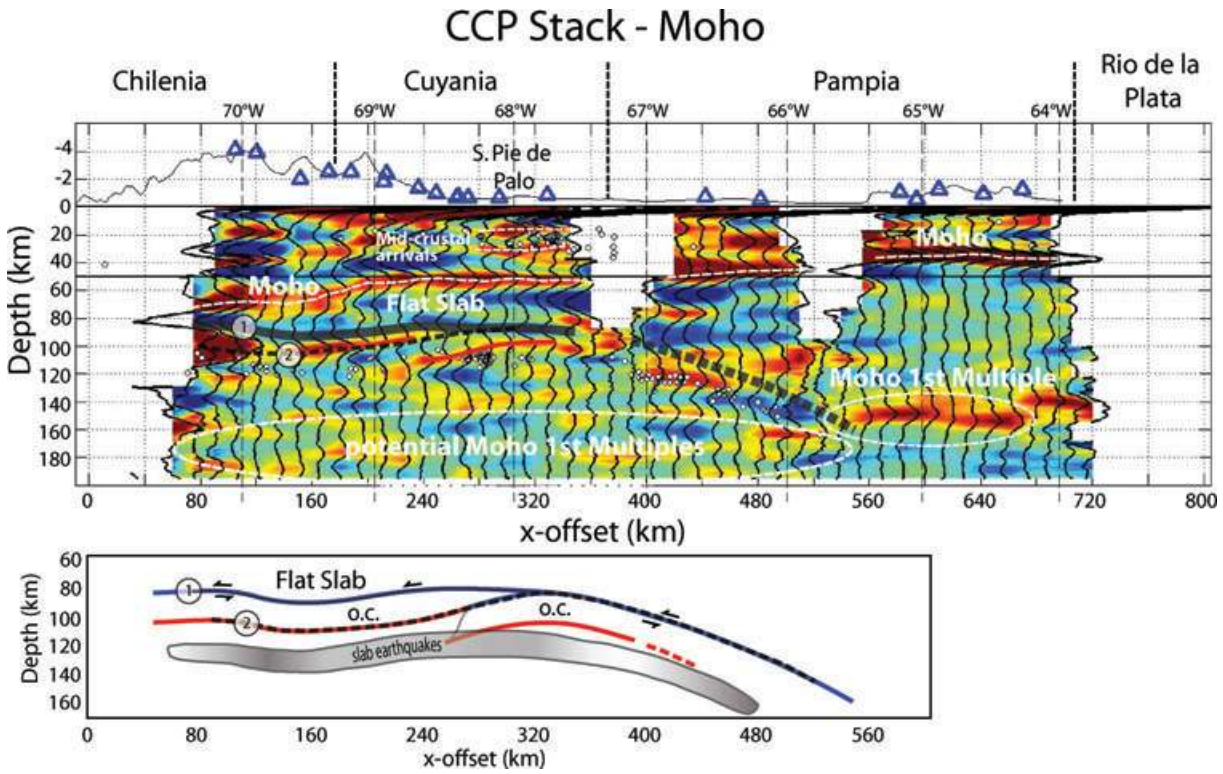

Figure 6. Top panel: CCP Stack along section shown in Fig. 2 that contains the most continuous slab seismicity from the flat slab region to depths of ∼180 km and the highest station coverage. Grey shaded line marks a possible location of the top of the slab (1) in the flat region (solid) and dipping region (dashed). Note slab seismicity is ∼20 km below the top of the slab and does not appear to be offset where the oceanic Moho is offset (red lines). The thin dashed line (top and bottom plots) marks an alternate possibility for the top of the slab (2) if a sliver of the slab was accreting to the bottom of the upper plate. Continental crustal thicknesses are greatest underneath the Andean Cordillera and Precordillera and shallow to the east. Blue triangles are seismic stations, white circles are earthquakes. Slab earthquakes occur predominantly in the oceanic mantle of the subducting slab. Note that Moho multiples are below interpreted flat slab. Bottom panel: cartoon showing two possible locations for the top of the subducting slab.

signal disappears in Y-Lines 20 and 21. These offsets are laterally extensive (spanning at least ∼125 km), and located in the region with the highest station coverage. We have over 150 traces per bin being stacked in the region with the offset (Fig. S1), and are confident that the offsets we are imaging in the flat slab region are real, and not due to near-surface velocity variations, for example.

Fig. 6 is a cross-section showing the most continuous slab seismicity from the flat slab region to depths of ∼180 km and having the highest station coverage. We note that the slab seismicity is not offset where we observe an offset in the oceanic Moho. We can interpret a relatively smooth interface about 10–20 km above the slab earthquakes as the active plate interface accommodating convergence between the two plates. Two possibilities for the plate interface are illustrated in Fig. 6: one at the top of the oceanic crust with internal deformation within the crust and the other cutting up from the base of the oceanic crust to the top, outlining a 'sliver' being transferred from the slab to the overlying plate. This type of tectonic underplating is observed at other subduction zones, although at shallower depths (e.g. Calvert *et al.* 2006). In either case, at some locations the interface is coincident with the top of the oceanic crust, but in other locations it may not be. We would expect that the plate interface at this depth is aseismic. The slab earthquakes appear to be occurring predominantly in the oceanic mantle part of the slab. Focal mechanisms of the larger slab earthquakes in the global CMT catalogues, as well as from slab events determined by Anderson *et al.* (2007), indicate mostly normal faulting with the T-axis oriented approximately north–south. These observations suggest the current slab seismicity reflects the present-day stress field within the slab, and that the oceanic crust offsets are not currently active.

The flat slab is visible for ∼200 km in the CCP stacks, before it fades at the region where the highest seismicity also ceases, around x-offset 320 km (Fig. 4) and Y-Line 20 (Fig. 5). When the oceanic crust begins to transform to eclogite, the velocity (and density) contrast between the oceanic crust and over- and underlying mantle diminishes, and thus the strong negative-to-positive conversions disappear. This transformation begins to occur just before the slab sinks back down at a normal dipping angle [outlined using the sparser, deeper seismicity, Anderson *et al.* (2007)], due to the increased density of eclogite (e.g. Abbott *et al.* 1994; Hacker *et al.* 2003a,b). Fig. 7(a) shows the depth to the top of the oceanic crust of the subducting slab, based on picks from the CCP stacks of the negative arrival, representing the top of the oceanic crust. When the slab signal disappears, we are unable to pick the negative arrival, and so we can infer the edge of the eclogite transformation region by the limit of the slab depth picks.

The offset in the top of the oceanic crust is well defined in Fig. 7(a). West of the offset, oceanic crust depths shallow from 96 to 83 km. East of the offset, the depth to the top of the oceanic crust drops to 109 km in the south, rising to 95 km at the northernmost offset. North of the direct path of the JFR, depths to the top of the oceanic crust level out, and range from 89 to 101 km. Where possible, minimum oceanic crustal thicknesses were then measured directly from the CCP stacks, and results are shown in Fig. 7(b).

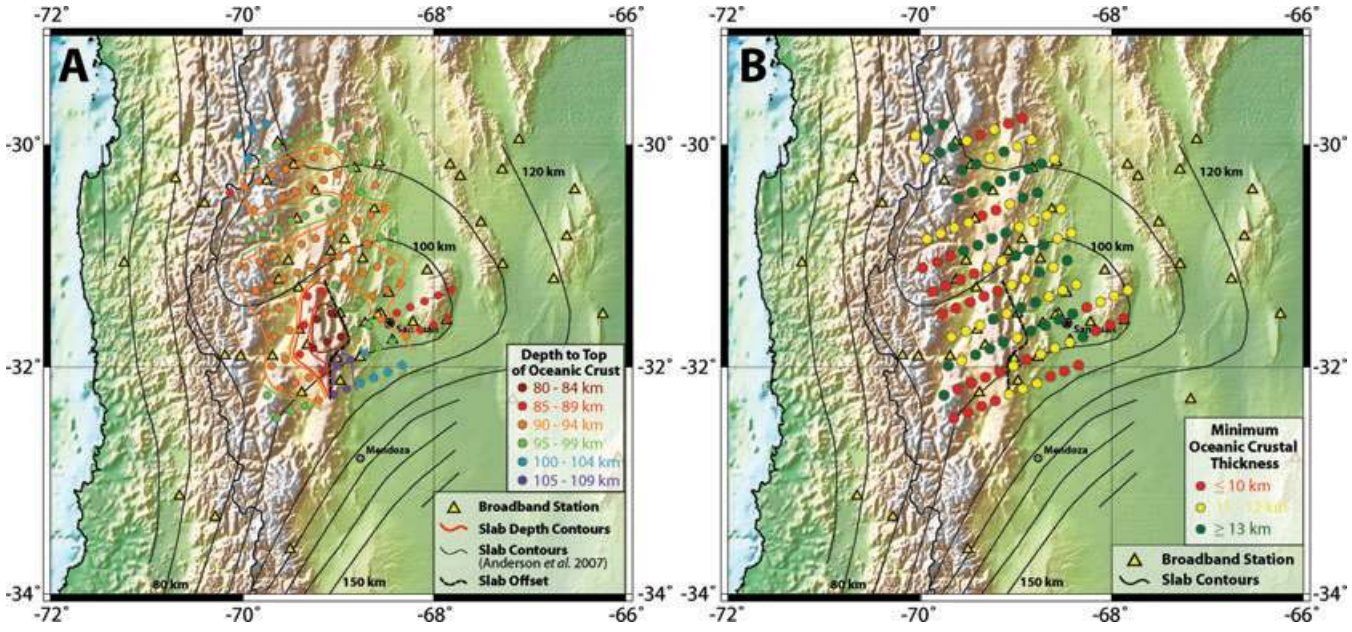

Figure 7. (A) Depth to top of the oceanic crust, based on picks from CCP stack results. Each circle represents a CCP trace at a node point. (B) Minimum oceanic crustal thicknesses beneath the Chilenia and Cuyania terranes, based on the CCP stacks. Offset in slab is shown by thick black dashed line. Previous slab contours from Anderson *et al.* (2007) are shown for comparison.

Because a higher average velocity of 8.0 km s^{-1} was used to migrate the CCP stacks in the mantle, the thicknesses measured from the traces will be smaller than they should be, as oceanic crustal velocities are slower than the surrounding mantle. Minimum oceanic crustal thicknesses range from 8 to 16 km, with ∼70 per cent greater than 11 km, and ∼40 per cent greater than 13 km. Based on synthetics and the traveltime equations of Zandt *et al*. (1995) to determine layer thickness, the underestimation of the crustal thicknesses is ∼20 per cent, assuming a V_p of 7.2 km s^{-1} in the subducted oceanic crust. Therefore, a CCP stack measured thickness of 11 km is actually 13 km thick, and 16 km becomes 19 km using the correct oceanic crust velocity. This means that more than 70 per cent of our measurements of oceanic crustal thickness are 13 km or greater. There does not appear to be a concentration of overthickened crust solely along the direct path of the JFR, implying that there is more likely a broad region of overthickened crust, not just along the volcanic chain, and that the flat slab itself may be broader than proposed by Anderson *et al.* (2007). Slab seismicity during the SIEMBRA and ESP experiments also supports this notion of a wider flat slab region, more closely following contours of Cahill & Isacks (1992). Unfortunately, there is not enough station coverage further north or south of our deployments to determine where the overthickened region ends.

Upper plate crustal structure

In addition to imaging the flat slab signal, we also see a distinct, but patchy, continental crustal Moho signal throughout the cross-sections. The depth to Moho is greatest in the west (upwards of ∼70 km beneath the Main Cordillera), and decreases to the east, reaching ∼35 km under the ESP stations. The observable Moho signal is complex, reflecting the complicated geology of the region. In Fig. 6, the Moho signal is strongest underneath the ESP stations, where it averages ∼40 km. Here, the crustal structure is simple, with a relatively flat-lying Moho. To the west, the strength of the Moho signal varies and occasionally disappears. We have also highlighted the first multiple of the Moho beneath the ESP stations, to demonstrate that the multiples from the Moho are not interfering with our interpreted flat slab signal (Fig. 6). For a ∼40 km deep Moho, the first multiple is located between 140 and 160 km depth (see also moveout plots in Fig. S3). In the west, the Moho is greater than 50 km, and thus the multiples are deeper than ∼160 km (Fig. 6), well below where we interpret the flat slab.

Beneath the basement-cored uplift of Sierra de Pie de Palo, there is a mid-crustal positive polarity arrival at ∼30 km depth, that extends ∼40 km to the west (Fig. 4), and the Moho appears at ∼50 km depth. There appears to be an increase in crustal seismicity in this region, as well (e.g. Gutscher 2002; Alvarado *et al.* 2005, 2009). This mid-crustal feature could be a decollement beneath the Sierra de Pie de Palo, as proposed by Cominguez & Ramos (1991), Ramos *et al.* (2002) and Regnier *et al.* (1992), and as imaged as a mid-crustal arrival in the CHARGE data at station JUAN by Calkins *et al.* (2006) and a station to the southwest of the Sierra de Pie de Palo by Perarnau *et al.* (2010). Regnier *et al.* (1992) proposed a decollement at 22–25 km, based on intraplate focal mechanisms, whereas Calkins *et al.* (2006) found a positive polarity arrival at 32 km and Perarnau *et al.* (2010) at 28 km. With our increased coverage, we were able to image this mid-crustal layer across several lines (X-Lines 11–13, Fig. 4; Y-Lines 18–21, Fig. 5), located at ∼30 km depth. We also imaged a strong positive arrival at ∼18 km depth beneath the Sierra de Pie de Palo; Calkins *et al.* (2006) similarly imaged a positive arrival at 20 km depth, based on higher-frequency local event RFs, and Perarnau *et al.* (2010) at 13 km based on teleseismic data from a nearby permanent station to the southwest of the range. Around 75 km south of Sierra de Pie de Palo, Cominguez & Ramos (1991) imaged two strong reflectors at ∼18 and ∼32 km using seismic reflection data. Zapata (1998) interpreted an Andean decollement at ∼13–20 km depth, dipping to the northeast, between the Eastern Precordillera and the Sierra de Valle Fértil (Fig. 1). It could be this decollement that is imaged at ∼18 km depth in the RFs below the Sierra de Pie de Palo and to the west (X-Lines 11–12, Fig. 4; Y-Lines 18–21, Fig. 5). However, more investigation is needed to explore

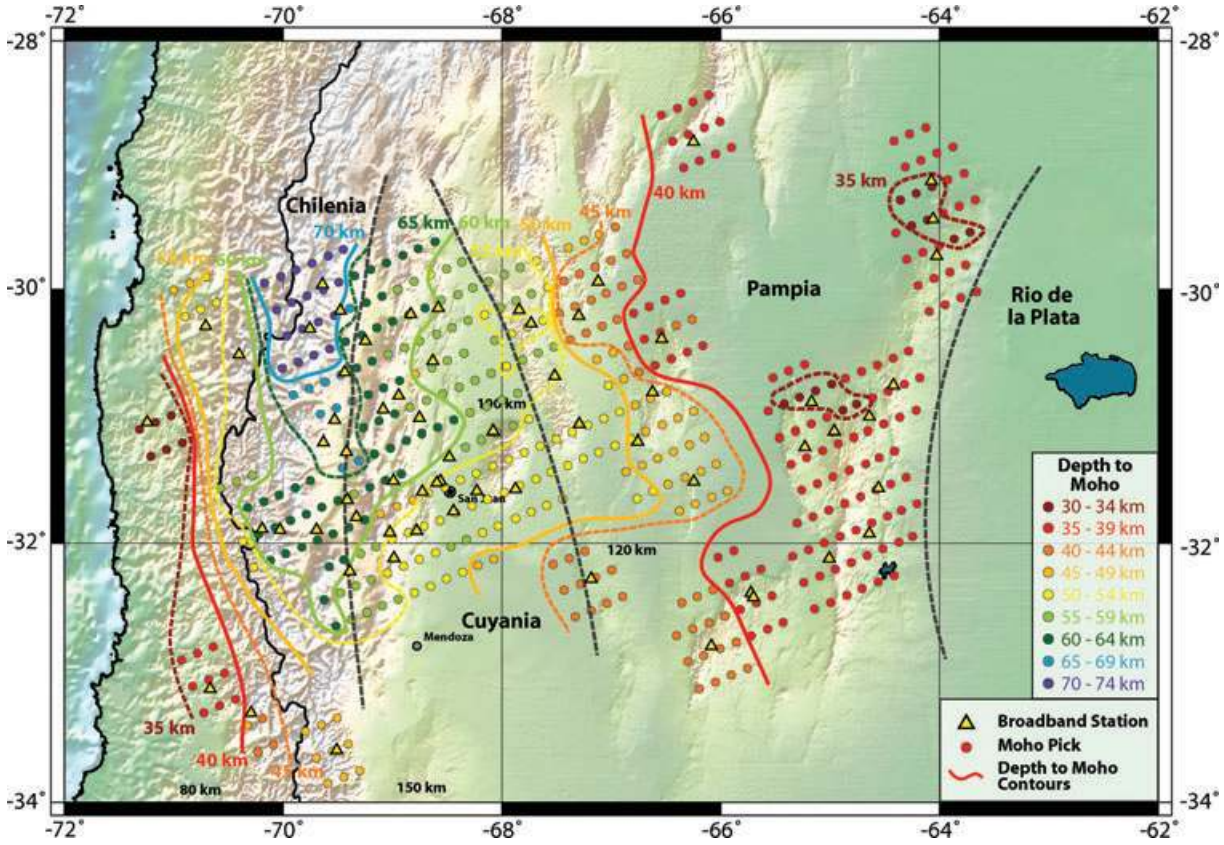

Figure 8. Depth to continental Moho map, based on picks from CCP Stack results, using only crustal velocities in the velocity model. Each circle represents a CCP trace at a node point. Greatest depths to Moho are found in the Principal and Frontal Cordilleras, and shallow to the east. Maximum and minimum depths to Moho are 73 and 32 km, respectively. Dark grey dashed lines are terrane boundaries. See text for details.

impedance changes related to mid-crustal discontinuities to see if they would produce a significant converted phase.

A depth to continental Moho map, based on RF Moho picks from the CCP stacks, is shown in Fig. 8. This new, higher resolution map improves upon the previous map of Alvarado *et al.* (2007) and sources therein. Moho depths match well those from Alvarado *et al.* (2007) in the eastern regions, below the ESP stations, but we find greater depths to Moho beneath the Cordilleras to the west, more than 70 km in places. Heit *et al.* (2008) found Moho depths of this magnitude (∼70 km) below the Precordillera, using *S*-wave RFs. Gilbert *et al.* (2006) had trouble imaging the Moho beneath the Precordillera, and attributed the lack of Moho signal to partial eclogitization of the lower crust. Their bin spacing was 50 km (versus our 15 km), however, and they had ∼10 per cent of the number of traces we used in our mesh. Because the Moho is structurally complicated in this region, it is possible that the lateral heterogeneities of the Moho would lead to incoherent stacking of Moho signal, which would cause the Moho to appear diminished in the stacks from Gilbert *et al.* (2006). As seen in Fig. 4, for example, the Moho is laterally variable in depth and signal strength. In X-Line 11, the Moho in the west jumps from 70 to 50 km over a short distance (30 to 40 km). Using Gilbert *et al.*'s (2006) bin spacing, the traces that are stacked within a bin would combine the 70 km arrival with the 50 km arrival, resulting in a weaker total stacked signal. It is still possible that the lower crust is partially eclogitized, however, as proposed by Gilbert *et al.* (2006). While absolute Moho depths can vary slightly based on the velocity model used in calculating the CCP stacks, the general lateral relationships will remain, assuming there are no lateral changes in velocity. In other words, regions that have a Moho deeper than the 50 km prescribed in the velocity model will have an artificially deep Moho in the stacks, as the Moho time will be migrated using an inappropriately fast mantle velocity, but the difference would be less than ∼5 km. To address this issue and determine more accurately the depth to Moho for Fig. 8, the CCP stacks were recalculated using just a crustal velocity of 6.2 km s^{-1}, as only the depth to Moho was picked. In the west, contour lines run mostly N–S, while to the east, the contour lines align more NW–SE and loosely align along terrane boundaries (Fig. 8).

DISCUSSION

The thickness of the oceanic crust of a subducting slab contributes to the overall buoyancy of the slab. A thicker layer of basaltic crust of the subducting slab, which is less dense than mantle peridotite (basalt is ∼400 kg m^{-3} less dense than the mantle) would increase the buoyancy of the slab. When the basalt layer converts to eclogite (which is ∼200 kg m^{-3} more dense than the mantle; Abbott *et al.* 1994), any additional buoyancy would be lost.

The buoyancy from a depleted region of the mantle that possesses less garnet (suboceanic lithospheric mantle) will act against the negative buoyancy of dense eclogite and so a very young (<5 Ma), hot, and thus buoyant, slab will tend to subduct horizontally (Abbott *et al.* 1994). For older oceanic crust (such as the 43 Ma Nazca Plate in our region), though, a sufficient amount of buoyant basaltic oceanic crust must be present for the slab to subduct horizontally. Van Hunen *et al.* (2002) modelled subduction of an 18-km-thick oceanic plateau, and found that the presence of a thickened basaltic plateau provides enough buoyancy to support the slab. These authors

found that flattening of a slab only occurs if the basalt-to-eclogite transition is inhibited by cooler temperatures. Once a slab begins to flatten, the cooler thermal structure of the more –closely coupled plates delays the basalt to eclogite transition by ∼8–10 Ma, allowing the flat portion of the slab to progress further inboard (Gutscher *et al.* 2000b). Gutscher *et al.* (2000b) used a simple isostatic model to show that for reasonable values of crustal and mantle materials, it is possible for a slab with an oceanic plateau of only 12 km to maintain neutral buoyancy, even for oceanic lithosphere with an age of 50 Ma. In order for a subducting slab to remain buoyant, the metastability of basaltic crust in the eclogite stability field is very important (van Hunen *et al.* 2002). Once this transition to eclogite occurs, the slab becomes too dense to remain buoyant and sinks down (or detaches) into the mantle.

To test whether the oceanic crust of the Nazca Plate along with the additional contribution of the JFR could achieve neutral, or even positive, buoyancy, we followed the methods of Cloos (1993) and Gutscher *et al.* (2000b) to calculate the minimum oceanic crustal thickness required. For 43 Ma oceanic lithosphere with a thickness of 75 km, buoyancy can be obtained with an oceanic crustal thickness of only 14 km, assuming a crustal density of 2900 kg m^{-3} and a lithospheric mantle density of 3300 kg m^{-3}. To determine buoyancy, or 'subductability', the mean bulk subducted lithospheric density was compared to the surrounding asthenosphere having a density of 3230 kg m^{-3} (Gutscher *et al.* 2000b), using the following formula

$$\text{buoyancy} = \rho_a - \left[\frac{(h_{oc} * \rho_{oc}) + ((h_{ol} - h_{oc}) * \rho_{lm})}{h_{ol}}\right], \quad (1)$$

where ρ_a, ρ_{oc} and ρ_{lm} are the densities of the asthenosphere, oceanic crust and lithospheric mantle in 10^3 kg m^{-3}, respectively, and h_{oc} and h_{ol} are the thicknesses of the oceanic crust and oceanic lithosphere in kilometres, respectively. Positive buoyancies indicate that the subducted slab will be able to support itself, and the minimum oceanic crustal thickness required to obtain this support is found at the transition between negative to positive buoyancies. For 40–50 Ma oceanic lithosphere with thicknesses ranging from 70 to 80 km, positive buoyancy can be obtained with a minimum oceanic crustal thickness of 13–14 km for the given bulk densities. The density contrasts that we use are similar to those used in other regional studies (e.g. Introcaso *et al.* 1992; Alvarado *et al.* 2009). The densities can vary, however, and Cloos (1993) notes that while the exact density values are not known, the contrasts (400 kg m^{-3} between bulk oceanic crustal and lithospheric mantle densities) are well determined. Based on our minimum oceanic crustal thickness estimates, over 70 per cent of crustal thickness picks are greater than 13 km.

To determine the thickness of the oceanic crust from our RFs using a second method, we compare our observed RF signals to synthetic RFs calculated using the waveform forward modelling code 'respknt' (Randall 1994). With this code, the response of a structure to an incident *P*-(or *S*-)wave can be computed, based on the reflectivity method assuming incident plane waves (Kennett 1983). Because we are trying to model the crustal thickness of a flat slab, the assumption of horizontal layers in the code is valid. Multiple traces from X-Lines 11 and 15 of the CCP stacks along the flat portion of the subducting slab were compared to synthetic RFs created with an input velocity model (Fig. 9). The negative-to-positive conversion that represents the oceanic crust was matched, and thus the layer thickness required to best match the CCP trace was determined. Oceanic crustal thicknesses calculated from the synthetics ranged from 13–15 km. In Fig. 9, four selected traces are shown, with thicknesses from 14 to 15 km. We fixed the continental crustal V_p at 6.2 km s^{-1}, and the upper mantle V_p at 8.0 km s^{-1}, and then varied the V_p of the oceanic crust to fit the signal from the top and bottom of the oceanic crust. The V_p of the oceanic crust as determined from synthetics ranges from 7.2 to 7.5 km s^{-1}. Based on the work of Hacker *et al.* (2003a), average oceanic crustal velocities can range from 6.6 –to 7.6 km s^{-1}. For appropriate P–T conditions in a flat slab region (400–800°C, 2–4 GPa; van Hunen *et al.* 2002; Gutscher *et al.* 2000a), Hacker *et al.* (2003a) predict *P*-wave velocities for unmetamorphosed MORB between ∼7.2 and 7.6 km s^{-1}. Our velocities fit within this range. The thicknesses of these same traces read directly from the CCP RF stacks are up to 3 km thinner than those found using synthetic modelling, confirming

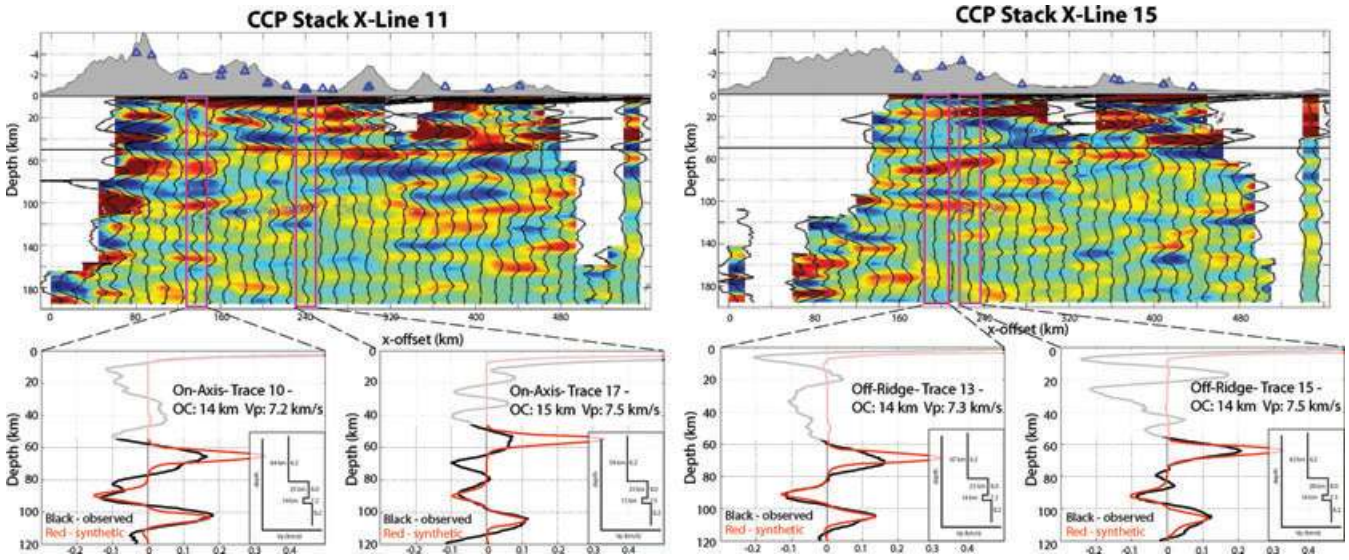

Figure 9. Sample synthetics of CCP traces (X-Lines 11 and 15, see Fig. 2) with the observed flat slab imaged. Traces outlined in magenta boxes are shown below. The negative-to-positive oceanic crust arrivals are matched using synthetics (respknt; Randall 1994), and the resulting best-match thicknesses and V_p value of the subducted crust are shown in the insets. Note that the crust was not modelled, so no attempt was made to match the amplitude of the continental Moho arrival. OC, oceanic crust.

that the measured oceanic crustal thicknesses from the CCP stacks are minimum estimates. There is a trade-off between oceanic crustal thickness and velocity, however, inherent in the non-uniqueness of modelling solutions. While the CCP traces can be fit with a 'normal' oceanic crustal thickness (∼8 km), the models used to achieve these results require an oceanic crustal velocity of ∼6.2 km s^{-1} and a V_p/V_s of ∼1.5, both of which are unreasonably low values (e.g. Hacker *et al.* 2003a).

One interpretation of an offset in the negative-to-positive arrival is that the oceanic crust along the direct path of the JFR is indeed broken or offset. There are several possible ways to have offsets in the top of the oceanic crust. First, there could be a reactivation of faults previously created offshore in the oceanic crust, prior to subduction. Such faults have been imaged offshore using multibeam bathymetry and are both trench parallel/perpendicular or aligned with the path of the JFR (Ranero *et al.* 2005). These faults commonly form due to bending of the plate (e.g. Fromm *et al.* 2006; Ranero *et al.* 2005), and could be reactivated by the bending of the slab as it becomes horizontal. Based on the strike of the offsets observed in the cross-sections (thick black dashed line, Fig. 7), the trench-subparallel faults observed offshore (F3 trench faults, Ranero *et al.* 2005) align most closely to the offsets in the slab. We do not have enough resolution in our CCP stacks, however, to interpret these offsets as normal or reverse faults. Another possible explanation for the offsets could be that the slab is newly broken due to the stresses induced by the increased coupling in the flat slab region. Gutscher (2002) points out that the largest seismic energy release is in flat slab regions, where there is the greatest coupling. In central Chile/Argentina, for example, the upper plate energy release associated with the Pampean flat slab region is five to ten times larger than along the rest of the Andean margin (Gutscher 2002). Increased coupling between the upper plate and the subducting slab could cause the flat slab to buckle, leading to the offsets observed in the RFs.

If tectonic underplating is occurring in this region of shallow subduction, then slivers of the upper part of the subducting Nazca Plate could be welded onto the base of the South American continental lithosphere (Cartoon, Fig. 6). Tectonic underplating has been observed, although generally at shallower depths, in subductions zones such as Alaska (Fuis *et al.* 2008), Cascadia (Calvert *et al.* 2006), Japan (Kimura *et al.* 2010) and New Zealand (Spasojevic & Clayton 2008). In Indonesia, Singh *et al.* (2008) seismically imaged broken oceanic crust and interpreted very strong coupling, which lead to brittle failure of mantle rocks in the subduction zone, and the great megathrust earthquake of 2004 in Sumatra.

Based on the RF analysis, the crustal structure is more complex in the west (Cuyania), than to the east (Pampia). Beneath the ESP stations, the Moho signal is strong and relatively flat lying. To the west, there are multiple mid-crustal structures apparent in the CCP stacks and the Moho signal is broken and variable in amplitude (Fig. 4). This complex Moho signal is above the region of the broken subducting slab (X-Line 11, Fig. 4). If there is increased coupling in this region, and tectonic underplating is occurring, then the Moho signal would be disjointed, as is observed. A detailed discussion of these features, however, is the focus of a future paper.

CONCLUSIONS

In this study, we used *P*-wave RFs to image the subsurface of the Pampean flat slab region beneath western Argentina. An improved depth to continental Moho map for the region has been obtained using our RF results. We find the greatest depths to Moho under the Main Cordillera (>70 km), which shallow to less than 40 km under the ESP. Moho contours tend to roughly follow terrane boundaries, running mostly N–S in the Cordilleras, and more NW–SE to the east, in the SP. This alignment indicates that the ancient terranes continue to exert control over present-day continental deformation. Further, there are several mid-crustal arrivals, two of which are prominent under the Sierra de Pie de Palo, at ∼18–32 km depth, and likely reflect the imbricated shallow structure and a decollement, respectively. We further achieved 3-D images of the subducting slab, and observed offsets in the flat slab portion directly along the path of the JFR. These offsets could possibly be due to: (1) reactivation of older faults in the oceanic crust, created when crust was first subducted, or (2) newer faults formed due to stresses induced by increased coupling in flat slab region, possibly due to tectonic underplating. Based on the results of the synthetic modelling combined with our RF analysis, we suggest that the Pampean flat slab is moderately overthickened, with the majority of oceanic crustal thicknesses ranging from 13 to 19 km. The oceanic crust is moderately overthickened over a broader region than aligned directly along the path of the JRF volcanic chain, implying that the overthickened oceanic crust influences a much broader region. This conclusion is supported by slab earthquake locations, which outline a flat surface over a greater area than the offshore volcanic line. These results support the idea of an overthickened oceanic crust as a contributing mechanism for flat slab subduction. In the Pampean flat slab region, with the overthickened subducted oceanic crust (13–19 km thick), combined with the westward overriding plate motion and possible upper mantle hydration as additional contributing factors, flat slab subduction is able to occur.

ACKNOWLEDGMENTS

We are grateful to IRIS and people at the PASSCAL Instrument Center for their help and support throughout the SIEMBRA deployment. The seismic instruments were provided by the Incorporated Research Institutions for Seismology (IRIS) through the PASSCAL Instrument Center (NSF Cooperative Agreement EAR-0552316). We also sincerely thank the Instituto Nacional de Prevención Sísmica, Argentina, for their help in logistics, as well as Noel Barstow (PASSCAL) for her invaluable assistance in the field. David Wilson, Ryan Porter, Michael McGlue and an anonymous reviewer are thanked for their detailed and thoughtful comments, which helped improve the quality of this manuscript. This research was supported by the National Science Foundation (EAR-0510966, EAR-0738935 and EAR-0739001) and FONCyT (Grant PICT06–0122). Maps were created using the Generic Mapping Tools (GMT) software (Wessel & Smith 1998).

REFERENCES

Abbott, D., Drury, R. & Smith, W.H.F., 1994. Flat to steep transition in subduction style, *Geology,* **22,** 937–940.

Abers, G.A., 2005. Seismic low-velocity layer at the top of subducting slabs: observations, predictions, and systematics, *Phys. Earth planet. Inter.,* **149,** 7–29.

Abers, G.A., van Keken, P.E., Kneller, E.A., Ferris, A. & Stachnik, J.C., 2006. The thermal structure of subduction zones constrained by seismic imaging: implications for slab dehydration and wedge flow, *Earth planet. Sci. Lett.,* **241,** 387–397.

Abers, G.A., MacKenzie, L.S., Rondenay, S., Zhang, Z., Wech, A.G. & Creager, K.C., 2009. Imaging the source region of Cascadia tremor and intermediate-depth earthquakes, *Geology,* **37,** 1119–1122.

Allmendinger, R.W., Figueroa, D., Snyder, D., Beer, J., Mpodozis, C. & Isacks, B.L., 1990. Foreland shortening and crustal balancing in the Andes at 30 degrees S latitude, *Tectonics,* **9,** 789–809.

Alvarado, P., Beck, S., Zandt, G., Araujo, M. & Triep, E., 2005. Crustal deformation in the south-central Andes backarc terranes as viewed from regional broad-band seismic waveform modelling, *Geophys. J. Int.,* **163,** 580–598, doi:10.1111/j.1365-246X.2005.02759.x.

Alvarado, P., Beck, S. & Zandt, G., 2007. Crustal structure of the south-central Andes Cordillera and backarc region from regional waveform modelling, *Geophys. J. Int.,* **170,** 858–875, doi:10.1111/j.1365-246X.2007.03452.x.

Alvarado, P., Pardo, M., Gilbert, H., Miranda, S., Anderson, M., Saez, M. & Beck, S., 2009. Flat-slab subduction and crustal models for the seismically active Sierras Pampeanas region of Argentina, in *Backbone of the Americas: Shallow Subduction, Plateau Uplift, and Ridge and Terrane Collision,* Geol. Soc. Am. Memoirs, Vol. 204, pp. 261–278, Geological Society of America, Boulder, CO.

Anderson, M., Alvarado, P., Zandt, G. & Beck, S., 2007. Geometry and brittle deformation of the subducting Nazca Plate, Central Chile and Argentina, *Geophys. J. Int.,* **171,** 419–434, doi:10.1111/j.1365-246X.2007.03483.x.

Audet, P., Bostock, M.G., Boyarko, D.C., Brudzinski, M.R. & Allen, R.M., 2010. Slab morphology in the Cascadia fore arc and its relation to episodic tremor and slip, *J. geophys. Res.,* **115,** doi:10.1029/2008JB006053.

Cahill, T. & Isacks, B., 1992. Seismicity and shape of the subducted Nazca plate, *J. geophys. Res.,* **97,** 17 503–17 529.

Calkins, J.A., Zandt, G., Gilbert, H.J. & Beck, S.L., 2006. Crustal images from San Juan, Argentina, obtained using high frequency local event receiver functions, *Geophys. Res. Lett.,* **33,** doi:10.1029/2005GL025516.

Calvert, A.J., Ramachandran, K., Kao, H. & Fisher, M.A., 2006. Local thickening of the Cascadia forearc crust and the origin of seismic reflectors in the uppermost mantle, *Tectonophysics,* **420,** 175–188.

Cloos, M., 1993. Lithospheric buoyancy and collisional orogenesis: subduction of oceanic plateaus, continental margins, island arcs, spreading ridges, and seamounts, *Geol. Soc. Am. Bull.,* **105,** 715–737.

Comínguez, A.H. & Ramos, V.A., 1991. La estructura profunda entre Precordillera y Sierras Pampeanas de la Argentina: Evidencias de la sísmica de reflexión profunda, *Rev. Geol. Chile,* **18,** 3–14.

DeCelles, P.G., 2004. Late Jurassic to Eocene Evolution of the Cordilleran thrust belt and foreland basin system, Western U.S.A., *Am. J. Sci.,* **304,** 105–168.

DeMets, C., Gordon, R.G. & Argus, D.F., 2010. Geologically current plate motions, *Geophys. J. Int.,* **181,** 1–80, doi:10.1111/j.1365-246X.2009.04491.x.

Dueker, K. & Sheehan, A., 1997. Mantle discontinuity structure from midpoint stacks of converted P to S converted waves across the Yellowstone hotspot track, *J. geophys. Res.,* **102,** 8313–8327.

Ferris, A., Abers, G.A., Christensen, D.H. & Veenstra, E., 2003. High resolution image of the subducted Pacific (?) plate beneath central Alaska, 50–150 km depth, *Earth planet. Sci. Lett.,* **214,** 575–588.

Fromm, R., Zandt, G. & Beck, S.L., 2004. Crustal thickness beneath the Andes and Sierras Pampeanas at 30°S inferred from Pn apparent phase velocities, *Geophys. Res. Lett.,* **31,** doi:10.1029/2003GL019231.

Fromm, R., Alvarado, P., Beck, S.L. & Zandt, G., 2006. The April 9, 2001 Juan Fernández Ridge (*M*w 6.7) tensional outer-rise earthquake and its aftershock sequence, *J. Seism.,* **10,** 163–170.

Fuis, G.S. *et al*., 2008. Trans-Alaska Crustal Transect and continental evolution involving subduction underplating and synchronous foreland thrusting, *Geology,* **36,** 267–270.

Gilbert, H.J. & Sheehan, A.F., 2004. Images of crustal variation in the intermountain west, *J. geophys. Res.,***109,** doi:10.1029/2003JB002730.

Gilbert, H., Beck, S. & Zandt, G., 2006. Lithospheric and upper mantle structure of central Chile and Argentina, *Geophys. J. Int.,* **165,** 383–398.

Gordillo, C.E. & Linares, A., 1981. Geocronología y petrografía de las vulcanitas terciarias del Departamento de Pocho. Provincia de Córdoba, *Revista de la Asociación Geológica Argentina,* **36,** 380–388.

Gripp, A.E. & Gordon, R.G., 2002. Young tracks of hotspots and current plate velocities, *Geophys. J. Int.,* **150,** 321–361.

Guillaume, B., Martinod, J. & Espurt, N., 2009. Variations of slab dip and overriding plate tectonics during subduction: insights from analogue modelling, *Tectonophysics,* **463,** 167–174.

Gurrola, H., Minster, J.B. & Owens, T., 1994. The use of velocity spectrum for stacking receiver functions and imaging upper mantle discontinuities, *Geophys. J. Int.,* **117,** 427–440.

Gutscher, M., 2002. Andean subduction styles and their effect on thermal structure and interplate coupling, *J. South Am. Earth Sci.,* **15,** 3–10.

Gutscher, M., Maury, R., Eissen, J.-P. & Bourdon, E., 2000a. Can slab melting be caused by flat subduction? *Geology,* **28,** 535–538.

Gutscher, M., Spakman, W., Bijwaard, H. & Engdahl, E.R., 2000b. Geodynamics of flat subduction: seismicity and tomographic constraints from the Andean margin, *Tectonics,* **19**(5), 814–833.

Hacker, B.R., Abers, G.A. & Peacock, S.M., 2003a. Subduction factory, 1, Theoretical mineralogy, densities, seismic wave speeds, and H_2O contents, *J. geophys. Res.,* **108,** doi:10.1029/2001JB001127.

Hacker, B.R., Peacock, S.M., Abers, G.A. & Holloway, S.D., 2003b. Subduction factory, 2, Are intermediate-depth earthquakes in subducting slabs linked to metamorphic dehydration reactions?, *J. geophys. Res.,* **108,** doi:10.1029/2001JB001129.

Heit, B., Yuan, X., Bianchi, M., Sodoudi, F. & Kind, R., 2008. Crustal thickness estimation beneath the southern central Andes at 30°S and 36°S from S wave receiver function analysis, *Geophys. J. Int.,* **174,** 249–254.

Helffrich, G., 1996. Subducted lithospheric slab velocity structure: observations and mineralogical inferences, *AGU Geophys. Monogr. Ser.,* **96,** 215–223.

Iidaka, T., Igarashi, T. & Iwasaki, T., 2009. Configuration of the subducting Philippine Sea slab in the eastern part of southwestern Japan with seismic array and Hi-net data, *Gondwana Res.,* **16,** 504–511.

Introcaso, A., Pacino, M.C. & Fraga, H., 1992. Gravity, isostasy and Andean crustal shortening between latitudes 30 and 35°S, *Tectonophysics,* **205,** 31–48.

Jones, C.H. & Phinney, R.A., 1998. Seismic structure of the lithosphere from teleseismic converted arrivals observed at small arrays in the southern Sierra Nevada and vicinity, California, *J. geophys. Res.,* **103,** 10 065–10 090.

Jordan, T.E. & Allmendinger, R.W., 1986. The Sierras Pampeanas of Argentina: a modern analogue of Rocky Mountain Foreland Deformation, *Am. J. Sci.,* **286,** 737–764.

Jordan, T.E., Isacks, B.L., Allmendinger, R.W., Brewer, J.A., Ramos, V.A. & Ando, C.J., 1983. Andean tectonics related to the geometry of the subducted Nazca Plate, *Geol. Soc. Am. Bull.,* **94,** 341–361.

Kawakatsu, H. & Watada, S., 2007. Seismic evidence for deep-water transportation in the mantle, *Science,* **316,** 1468–1471.

Kay, S., Mpdozis, C., Ramos, V. & Munizaga, F., 1991. Magma source variations for mid-late Tertiary magmatic rocks associated with a shallowing subduction zone and a thickening crust in the central Andes (28 to 33°S), in *Andean Magmatism and its Tectonic Setting*, Geol. Soc. Am. Spec. Pub., Vol. 265, pp. 113–137, eds. Harmon, R.S. & Rapela, C.W., Geological Society of America, Boulder, CO.

Kay, S.M. & Abbruzzi, J.M., 1996. Magmatic evidence for Neogene lithospheric evolution of the central Andean "flat-slab" between 30° S and 32° S, *Tectonophysics,* **259,** 15–28.

Kay, S.M. & Gordillo, C.E., 1994. Pocho volcanic rocks and the melting of depleted continental lithosphere above a shallowly dipping subduction zone in the Central Andes, *Contrib. Min. Pet.,* **117,** 25–44.

Kay, S.M. & Mpodozis, C., 2002. Magmatism as a probe to the Neogene shallowing of the Nazca plate beneath the modern Chilean flat-slab, *J. South Am. Earth Sci.,* **15,** 39–57.

Kennett, B.L.N., 1983. Approximations to the response of the stratification, in *Seismic Wave Propagation in Stratified Media,* Cambridge University Press, Cambridge, 497 pp.

Kim, Y., Clayton, R.W. & Jackson, J.M., 2010. Geometry and seismic properties of the subducting Cocos plate in central Mexico, *J. geophys. Res.,* **115,** doi:10.1029/2009JB006942.

Kimura, H., Takeda, T., Obara, K. & Kasahara, K., 2010. Seismic evidence for active underplating below the megathrust earthquake zone in Japan, *Science,* **329,** 210–212.

Kopp, H., Flueh, E.R., Papenberg, C. & Klaeschen, D., 2004. Seismic investigations of the O'Higgins Seamount Group and Juan Fernándezh Ridge: aseismic ridge emplacement and lithosphere hydration, *Tectonics,* **23,** doi:10.1029/2003TC001590.

Langston, C.A., 1977. The effect of planar dipping structure on source and receiver responses for constant ray parameter, *Bull. seism. Soc. Am.,* **67,** 1029–1050.

Lienert, B.R., Berg, E. & Frazer, L.N., 1986. Hypocenter: an earthquake location method using centered, scaled, and adaptively damped least squares, *Bull. seism. Soc. Am.,* **76,** 771–783.

Ligorria, J. & Ammon, C.J., 1999. Iterative deconvolution and receiver-function estimation, *Bull. seism. Soc. Am.,* **89,** 1395–1400.

Martinod, J., Funiciello, F., Faccenna, C., Labanieh, S. & Regard, V., 2005. Dynamical effects of subducting ridges: insights from 3-D laboratory models, *Geophys. J. Int.,* **163,** 1137–1150.

McGeary, S., Nur, A. & Ben-Avraham, Z., 1985. Spatial gaps in arc volcanism: the effect of collision or subduction of oceanic plateaus, *Tectonophysics,* **119,** 195–221.

Owens, T.J., Zandt, G. & Taylor, S.R., 1984. Seismic evidence for an ancient rift beneath the Cumberland Plateau, Tennessee: a detailed analysis of broadband teleseismic *P* waveforms, *J. geophys. Res.,* **89,** 7783–7795.

Perarnau, M., Alvarado, P. & Saez, M., 2010. Estimación de la estructura cortical de velocidades sísmicas en el suroeste de la Sierra de Pie de Palo, provincia de San Juan, *Revista de la Asociación Geológica Argentina,* **67**(4), 473–480.

Perez-Campos, X. *et al*., 2008. Horizontal subduction and truncation of the Cocos Plate beneath central Mexico, *Geophys. Res. Lett.,* **35,** doi:10.1029/2008GL035127.

Pilger, R.H., 1981. Plate reconstructions, aseismic ridges, and low-angle subduction beneath the Andes, *Geol. Soc. Am. Bull.,* **92,** 448–456.

Ramos, V.A., 2009. Anatomy and global context of the Andes: main geologic features and the Andean orogenic cycle, in *Backbone of the Americas: Shallow Subduction, Plateau Uplift, and Ridge and Terrane Collision,* Geol. Soc. Am. Memoir, Vol. 204, pp. 31–65, Geological Society of America, Boulder, CO.

Ramos, V.A., Cegarra, M. & Cristallini, E.O., 1996. Cenozoic tectonics of the High Andes of west-central Argentina (30–36°S latitude), *Tectonophysics,* **259,**185–200.

Ramos, V.A., Cristallini E.O. & Perez, D.J., 2002. The Pampean flat-slab of the Central Andes, *J. South Am. Earth Sci.,* **15,** 59–78.

Ramos, V.A., Vujovich, G., Martino, R. & Otamendi, J., 2010. Pampia: a large cratonic block missing in the Rodinia supercontinent, *J. Geodyn.,* **50,** 243–255.

Randall, G.E., 1994. Efficient calculation of complete differential seismograms for laterally homogeneous earth models, *Geophys. J. Int.,* **118,** 245–254.

Ranero, C.R., Villasenor, A., Phipps Morgan, J. & Weinrebe, W., 2005. Relationship between bend-faulting at trenches and intermediate-depth seismicity, *Geochem. Geophys. Geosys.,* **6**(12), doi:10.1029/2005GC000997.

Rapela, C.W., Pankhurst, R.J., Casquet, C., Baldo, E., Saavedra, J. & Galindo, C., 1998. Early evolution of the Proto-Andean margin of South America, *Geology,* **26,** 707–710.

Rapela, C.W., Pankhurst, R.J., Casquet, C., Fanning, C.M., Baldo, E.G., González-Casado, J.M., Galindo, C. & Dahlquist, J., 2007. The Río de la Plata craton and the assembly of SW Gondwana, *Earth Sci. Rev.,* **83,** 49–82.

Regnier, M., Chatelain, J.L., Smalley, R., Chiu, J.-M., Isacks, B.L. & Araujo, M., 1992. Seismotectonics of Sierra Pie de Palo, a basement block uplift in the Andean foreland of Argentina, *Bull. seism. Soc. Am.,* **82,** 2549–2571.

Saleeby, J., 2003. Segmentation of the Laramide Slab – evidence from the southern Sierra Nevada region, *Geol. Soc. Am. Bull.,* **115,** 655–668.

Singh, S.C. *et al.*, 2008. Seismic evidence for broken oceanic crust in the 2004 Sumatra earthquake epicentral region, *Nat. Geosci.,* **1,** 777–781, doi:10.1038/ngeo336.

Song, T.A., Helmberger, D.V., Brudzinski, M.R., Clayton, R.W., Davis, P., Perez-Campos, X. & Singh, S.K., 2009. Subducting slab ultra-slow velocity layer coincident with silent earthquakes in southern Mexico, *Science,* **324,** 502–506.

Spasojevic, S. & Clayton, R.W., 2008. Crustal structure and apparent tectonic underplating from receiver function analysis in South Island, New Zealand, *J. geophys. Res.,* **113,** doi:10.1029/2007JB005166.

Tibi, R., Wiens, D.A. & Yuan, X., 2008. Seismic evidence for widespread serpentinized forearc mantle along the Mariana convergence margin, *Geophys. Res. Lett.,* **35,** doi:10.1029/2008GL034163.

Urbina, N., Sruoga P. & Malvicini, L., 1997. Late Tertiary gold-bearing volcanic belt in the Sierras Pampeanas of San Luis, Argentina, *Int. Geol. Rev.,* **39,** 287–306.

Van Hunen, J., van den Berg, A.P. & Vlaar, N.J., 2002. On the role of subducting oceanic plateaus in the development of shallow flat subduction, *Tectonophysics,* **352,** 317–333.

Van Hunen, J., van den Berg, A.P. & Vlaar, N.J., 2004. Various mechanisms to induce present-day shallow flat slab subduction and implications for the younger Earth: a numerical parameter study, *Phys. Earth planet. Int.,* **146,** 179–194.

Wessel, P. & Smith, W.H.F., 1998. New, improved version of the Generic Mapping Tools released, *EOS, Trans. Am. geophys. Un.,* **79,** 579.

Yáñez, G.A., Ranero, C.R., von Huene, R. & Díaz, J., 2001. Magnetic anomaly interpretation across the southern central Andes (32°–34°S): the role of the Juan Fernández Ridge in the late Tertiary evolution of the margin, *J. geophys. Res.,* **106,** 6325–6345.

Yáñez, G., Cembrano, J., Pardo, M., Ranero, C. & Selles, D., 2002. The Challenger–Juan Fernández–Maipo major tectonic transition of the Nazca–Andean subduction system at 33–34°S: geodynamic evidence and implications, *J. South Am. Earth Sci.,* **15,** 23–38.

Yuan, X. *et al*., 2000. Subduction and collision processes in the Central Andes constrained by converted seismic phases, *Nature,* **408,** 958–961.

Zandt, G., Myers, S. & Wallace, T.C., 1995. Crust and mantle structure across the Basin and Range—Colorado Plateau boundary at 37°N latitude and implications for Cenezoic extensional mechanism, *J. geophys. Res.,* **100,** 10 529–10 548.

Zapata, T.R., 1998. Crustal structure of the Andean thrust front at 30°latitude from shallow and deep seismic reflection profiles, Argentina, *J. South Am. Earth Sci.,* **11,** 131–151.

SUPPORTING INFORMATION

Additional Supporting Information may be found in the online version of this article:

Figure S1. Selected SW–NE Ray Density Plots for corresponding CCP RF stacks.
Figure S2. Comparison of unnormalized versus normalized data in CCP RF stacks.
Figure S3. Moveout plots for three ESP stations at a Gaussian of 2.5.

Please note: Wiley-Blackwell are not responsible for the content or functionality of any supporting materials supplied by the authors. Any queries (other than missing material) should be directed to the corresponding author for the article.